Available online at www.sciencedirect.com
ScienceDirect
Energy Reports 9 (2023) 748–756
www.elsevier.com/locate/egyr

2022 The 3rd International Conference on Power and Electrical Engineering (ICPEE 2022)
29–31 December, Singapore

A new stationary frame multi-input multi-output EMT-level frequency scanning method for inverter based resources

Lei Meng[a], Ulas Karaagac[a,*], Mohsen Ghafouri[b], Anton Stepanov[c], Jean Mahseredjian[c]

[a] *Department of Electrical Engineering, The Hong Kong Polytechnic University, Hung Hom, Kowloon, Hong Kong*
[b] *Concordia Institute for Information Systems Engineering, Concordia University, Montreal, QC, Canada*
[c] *Department of Electrical Engineering, Polytechnique Montréal, Montreal, QC, Canada*

Received 18 April 2023; accepted 20 May 2023
Available online 3 June 2023

Abstract

Impedance-based stability analysis (IBSA) is an effective method to identify subsynchronous interaction (SSI) problem between the inverter-based resources (IBRs) and series compensated or weakly tied AC grids. The electromagnetic transient (EMT) level positive sequence and dq-frame frequency scanning methods (p-scan and dq-scan, respectively) are used to obtain the sequence single-input single-output (SISO) and dq multi-input multi-output (MIMO) impedance of IBRs, respectively. The dq MIMO impedance usage in IBSA provides more accurate results compared to the sequence SISO impedance. This paper proposes an EMT-level $\alpha\beta$-frame frequency scanning method ($\alpha\beta$-scan) to obtain the $\alpha\beta$ MIMO impedance and its usage in IBSA. The $\alpha\beta$-scan requires significantly less time compared to dq-scan for the convergence of MIMO IBR impedance representation and offers similar accuracy with dq-scan in IBSA. The accuracy of the proposed $\alpha\beta$ MIMO IBSA is validated by comparing with dq MIMO IBSA and EMT simulations on series capacitor SSI cases with different type IBRs (Doubly-fed induction generator (DFIG)-based wind park (WP) and full-scale converter (FSC)-based WP). This paper also uses a multivariable structure function(MSF)-based method for the first time in IBSA of SSI to achieve Bode plot-based analysis for providing better visualized presentation of resonance frequency and stability margins compared to generalized Nyquist criterion.

Peer-review under responsibility of the scientific committee of the 3rd International Conference on Power and Electrical Engineering, ICPEE, 2022.

Keywords: $\alpha\beta$-frame; $\alpha\beta$ MIMO impedance; EMT-level frequency scanning; IBSA; Inverter based resource; Stationary frame

1. Introduction

Recent studies have shown that the controllers of IBRs can adversely interact with the series compensated or weakly tied AC grids at subsynchronous frequency range [1–6]. This phenomenon is called subsynchronous interaction (SSI) and is confirmed with several real-life incidents [1]. Therefore, there has been a growing interest in developing effective SSI identification tools and mitigation methods.

* Corresponding author.
E-mail address: ulas.karaagac@polyu.edu.hk (U. Karaagac).

https://doi.org/10.1016/j.egyr.2023.05.129

Peer-review under responsibility of the scientific committee of the 3rd International Conference on Power and Electrical Engineering, ICPEE, 2022.

Various methods are used in literature to investigate the stability issues related to IBRs, such as the state-space-based assessment (SSA) [4–7], impedance based stability analysis (IBSA) [8–13], and electromagnetic transient (EMT) simulation-based assessment [14,15]. SSA is an effective way for interpreting the instability mechanism as the impact factors can be identified according to the participation of each state variable to dominant eigenvalues [7]. However, it has accuracy problem due to simplifications while obtaining the linearized system model [4–7]. Moreover, its application to large-scale power systems is not practical [2,3]. Therefore, SSA is mainly used for SSI mitigation design rather than SSI identification.

IBSA recently gained popularity due to its simplicity and applicability to large-scale power systems [2,3]. The desired accuracy can be achieved when the frequency dependent IBR impedance is extracted using EMT-level simulations instead of simplified analytical models. This method also allows extracting impedance characteristics of manufacturer-specific models, hence widely used by the transmission system operators (TSOs) [3,11–13]. EMT simulation based assessment is typically performed for representative scenarios to validate either the SSA or IBSA results.

The positive sequence frequency scanning (p-scan) is used to extract the single-input single-output (SISO) impedance of IBRs for IBSA. This method is widely used by TSOs due to its simplicity [3,11–13]. However, it has accuracy problem as the phase locked loop (PLL) and different outer loop control strategies in d- and q- axes channels lead to an asymmetry and cross couplings in the impedance characteristics of IBR [16]. In [17–22], the dq rotating reference frame (dq-frame) multi-input multi-output (MIMO) model is developed for ultimate accuracy in IBSA where the EMT-level dq-frame frequency scanning (dq-scan) is used to extract the IBR impedance model.

This paper proposes an EMT-level $\alpha\beta$-frame frequency scanning method ($\alpha\beta$-scan) to obtain $\alpha\beta$ MIMO impedance and its usage in IBSA. The $\alpha\beta$-scan requires significantly less time compared to dq-scan for the convergence of MIMO IBR admittance representation. Moreover, $\alpha\beta$ MIMO impedance usage in IBSA provides similar accuracy with dq MIMO impedance [23,24].

The generalized Nyquist criterion (GNC) is typically used in MIMO IBSA of SSI [25]. However, the resonance frequency and stability margins cannot be directly observed in the Nyquist diagrams. Bode plot provides direct visualized presentation of resonance frequency and stability margins, but only works for SISO IBSA. The multivariable structure function (MSF) was first established for individual channel design in close-loop control systems [26,27], in which couplings of the system are considered. In this paper, the MSF is used for the first time in the MIMO IBSA of SSI. In MSF-based analysis, the 2×2 system consisting of the $\alpha\beta$ impedance of grid and $\alpha\beta$ admittance of IBR is separated into two individual channels, and the stability of each channel is analyzed through Bode plot.

The paper is organized as follows. In Section 2, $\alpha\beta$-scan procedure is introduced, then the GNC and MSF-based $\alpha\beta$ MIMO IBSA methods are presented briefly. In Section 3, the accuracy of $\alpha\beta$ MIMO IBSA is validated by comparing with dq MIMO IBSA and EMT simulations on series capacitor SSI cases with different type IBRs (Doubly-fed induction generator (DFIG) based wind park (WP) and full-scale converter (FSC) based WP). Section 4 concludes the paper.

2. Multivariable IBSA in $\alpha\beta$-frame

2.1. EMT-level IBR side $\alpha\beta$-scan

The schematic diagram of IBR side $\alpha\beta$-scan is shown in Fig. 1. Single-tone voltage perturbations are applied to obtain the $\alpha\beta$-frame IBR admittance $\mathbf{Y}_{\alpha\beta}^{\mathbf{IBR}}(f_i)$, where f_i is the perturbation voltage frequency. The transmission grid is represented with a voltage source ($\mathbf{v_0} = v_{\alpha 0} + jv_{\beta 0}$) behind the Thevenin equivalent impedance ($\mathbf{Z_{sys}}$) at 60 Hz. EMT-type simulation programs have specific initialization methods for the IBR and certain time is needed for initialization transients to vanish. To improve the simulation efficiency, the system snapshot is taken in the first simulation when it reaches to steady state condition and used in the following voltage perturbation simulations. The $\alpha\beta$-scan procedure is as follows:

- The appropriate single-tone sinusoidal perturbations v_{pert}^{α} and v_{pert}^{β} are separately applied on top of $[0 \quad v_{\alpha 0} \quad v_{\beta 0}]^T$.
- The $\alpha\beta$-frame signals are transformed into abc-frame and injected to the system through controlled voltage source.

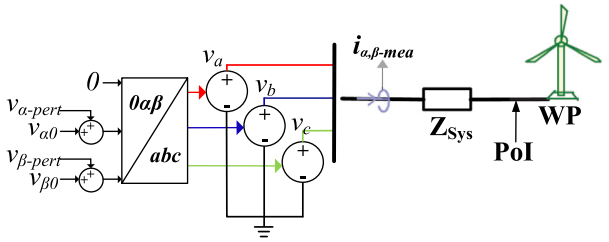

Fig. 1. Schematic diagram of voltage perturbation based $\alpha\beta$-scanning method.

- Three-phase currents are measured at the point of injection and transformed back to $\alpha\beta$-frame. The discrete Fourier transform (DFT) analysis is applied to extract the frequency spectrum of the current measurements. It should be noted that the DFT window should span an integer number of the cycles of fundamental, perturbation, and the corresponding mirror frequencies in order to prevent spectral leakage in DFT. The $\alpha\beta$-frame admittance components of IBR are found by:

$$\begin{aligned}
Y_{\alpha\alpha}^{IBR}(f_i) &= \frac{\left|I_{\alpha-mea}^{\alpha}(f_i)\right|}{\left|V_{pert}^{\alpha}(f_i)\right|}\left(\angle I_{\alpha-mea}^{\alpha}(f_i) - \angle V_{pert}^{\alpha}(f_i)\right),\\
Y_{\beta\alpha}^{IBR}(f_i) &= \frac{\left|I_{\beta-mea}^{\alpha}(f_i)\right|}{\left|V_{pert}^{\alpha}(f_i)\right|}\left(\angle I_{\beta-mea}^{\alpha}(f_i) - \angle V_{pert}^{\alpha}(f_i)\right),\\
Y_{\alpha\beta}^{IBR}(f_i) &= \frac{\left|I_{\alpha-mea}^{\beta}(f_i)\right|}{\left|V_{pert}^{\beta}(f_i)\right|}\left(\angle I_{\alpha-mea}^{\beta}(f_i) - \angle V_{pert}^{\beta}(f_i)\right),\\
Y_{\beta\beta}^{IBR}(f_i) &= \frac{I_{\beta-mea}^{\beta}(f_i)}{\left|V_{pert}^{\beta}(f_i)\right|}\left(\angle I_{\beta-mea}^{\beta}(f_i) - \angle V_{pert}^{\beta}(f_i)\right)
\end{aligned} \tag{1}$$

where $|\cdot|$ and $\angle$ indicate magnitude and phase angle of a phasor, respectively; subscripts α-*mea* and β-*mea* in I indicate the measured current components in α- and β- frames, respectively; and superscripts α and β of I and V indicate on which axis the voltage perturbation is injected.

Convergence criteria are set to ensure that the variations in magnitude and phase angle of each impedance component are negligible. The convergence criteria for $Y_{\alpha\beta-IBR}(f_i)$ is below:

$$\frac{\left|\Delta Mag\left(Y_{\alpha\beta-IBR}(f_i)\right)\right|}{\left|Mag\left(Y_{\alpha\beta-IBR}(f_i)\right)\right|} < tol \qquad \& \qquad \frac{\left|\Delta Ang\left(Y_{\alpha\beta-IBR}(f_i)\right)\right|}{\left|Ang\left(Y_{\alpha\beta-IBR}(f_i)\right)\right|} < tol \tag{2}$$

where ΔMag and ΔAng are variations of magnitude and phase angle of IBR admittance components in user specified time period, respectively; *tol* is convergence tolerance value. Once the convergence criteria are met, $\alpha\beta$-scan tool stops the EMT simulation, record the impedance for post-processing and repeat the simulation for the next frequency.

2.2. Extraction of grid side $\alpha\beta$-frame impedance using phasor solution-based frequency scanning tool

Grid side impedance is typically obtained using the phasor solution-based frequency-scanning tool available in EMT type programs while screening SSI risk in large-scale power systems [3]. The IBRs inside the grid side subsystem are typically represented with their frequency-dependent impedance tables, which are obtained through EMT-level frequency scanning [3]. Then the sequence domain grid side impedances are transformed into $\alpha\beta$-frame using [28]:

$$\mathbf{Z}_{\boldsymbol{\alpha\beta}}^{\mathbf{Grid}}(f_i) = diag\left(\left[Z_{\alpha\alpha}^{Grid}(f_i) \quad Z_{\beta\beta}^{Grid}(f_i)\right]\right) = \underbrace{\frac{1}{2}\begin{bmatrix}1 & 1\\ -j & j\end{bmatrix}}_{\mathbf{C^{-1}}} diag\left(\left[Z_{p}^{Grid}(f_i) \quad Z_{n}^{Grid}(f_i)\right]\right) \underbrace{\begin{bmatrix}1 & j\\ 1 & -j\end{bmatrix}}_{\mathbf{C}} \tag{3}$$

where $Z_p^{Grid}(f_i)$, and $Z_n^{Grid}(f_i)$ are the positive and negative sequence grid impedances, respectively. As the grid side subsystem is sequence decoupled, its $\alpha\beta$-frame impedance is a diagonal matrix.

2.3. MIMO IBSA methods

2.3.1. IBSA with GNC

The GNC is widely used for MIMO IBSA [25]. The $\alpha\beta$ impedance-based closed-loop transfer function of the whole system is given as [29]:

$$\mathbf{H}(j\omega) = \mathbf{Y}_{\alpha\beta}^{\mathbf{IBR}}(j\omega) \Big/ \left(\mathbf{I} + \mathbf{Z}_{\alpha\beta}^{\mathbf{Grid}}(j\omega)\,\mathbf{Y}_{\alpha\beta}^{\mathbf{IBR}}(j\omega)\right) \tag{4}$$

where $\omega = 2\pi f$ is the angular frequency. The system is stable if the encirclement of eigenvalue-loci of $\mathbf{Z}_{\alpha\beta}^{\mathbf{Grid}}(j\omega)\,\mathbf{Y}_{\alpha\beta}^{\mathbf{IBR}}(j\omega)$ to $(-1, \text{j}0)$ is zero under following assumptions: (i) the grid voltage is stable without IBR, (ii) the IBR is stable when connected to ideal voltage source [29].

2.3.2. IBSA with MSF

The MSF [26,27] is used in the MIMO IBSA of SSI. This method decouples the MIMO system, and provides the stability of each individual channel [26]:

$$\begin{aligned} F_{C1}(s) &= Z_{\alpha\alpha}^{Grid}(s)\, Y_{\alpha\alpha}^{IBR}(s)\,(1 - \gamma(s)\, h_2(s)) \\ F_{C2}(s) &= Z_{\beta\beta}^{Grid}(s)\, Y_{\beta\beta}^{IBR}(s)\,(1 - \gamma(s)\, h_1(s)) \end{aligned} \tag{5}$$

where γ, h_1, and h_2 are defined as:

$$\begin{aligned} \gamma(s) &= \left(Y_{\alpha\beta}^{IBR}(s)\, Y_{\beta\alpha}^{IBR}(s)\right) \Big/ \left(Y_{\alpha\alpha}^{IBR}(s)\, Y_{\beta\beta}^{IBR}(s)\right) \\ h_1(s) &= Z_{\alpha\alpha}^{Grid}(s)\, Y_{\alpha\alpha}^{IBR}(s) \Big/ \left(1 + Z_{\alpha\alpha}^{Grid}(s)\, Y_{\alpha\alpha}^{IBR}(s)\right), \\ h_2(s) &= Z_{\beta\beta}^{Grid}(s)\, Y_{\beta\beta}^{IBR}(s) \Big/ \left(1 + Z_{\beta\beta}^{Grid}(s)\, Y_{\beta\beta}^{IBR}(s)\right) \end{aligned} \tag{6}$$

The resonance frequency and stability margins can be obtained through Bode plot-based analysis to $F_{C1}(s)$ and $F_{C2}(s)$.

3. Case study

The benchmark in [22] is adopted for validation (see Fig. 2). The WP is radially connected to 230 kV strong system through series connected identical 50 km transmission lines (Line-1 and Line-2). A series capacitor is connected at the system side of the Line-2. Its value changes with parameter k as shown below:

$$|X_C| = k\,|X_{Line}|$$

where X_{Line} is the total impedance of Line-1 and Line-2, $X_C = 1/(j\omega_b C)$ is the impedance of series capacitor (C) at fundamental frequency ($\omega_b = 2\pi \times 60$).

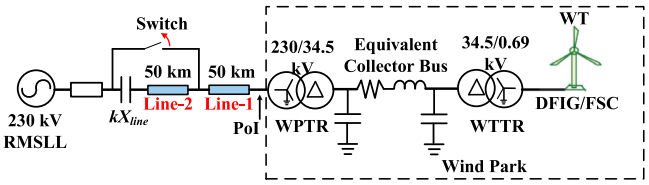

Fig. 2. Single line diagram of the system under study.

The considered cases are presented in Table 1. In cases 1 and 2, the WP consists of 66 DFIG-based wind turbines (WTs), each one with 1.7 MW power rating. In cases 3 and 4, the WPs consist of 50 and 200 FSC-based WTs (2 MW each), respectively. The hypothetical switch bypasses Line-2 and series capacitor. Opening that bypass switch causes series capacitor SSI in cases 2 and 4. The FSC- and DFIG-based WP models used in the paper are based on [30,31], respectively. [30] was developed by the IEEE Task Force for EMT-type modeling of WT generators and

Table 1. Study cases.

Case	WT type	Series compensation	WP size	EMT simulation
1	DFIG	9% of X_{Line}	66 × 1.7 MW	Stable
2		10% of X_{Line}		Unstable
3	FSC	50% of X_{Line}	50 × 2 MW	Stable
4			200 × 2 MW	Unstable

parks. [31] was validated with field measurements in [32]. Those models are recommended to use in SSI studies in [33]. Readers should refer to [30,31] for details about the configurations and control schemes of WTs, and [22] for parameters of the benchmark.

EMTP-RV [34] is used for impedance scans and EMT validation with 50 μs simulation time step. In $\alpha\beta$-scan, the $\alpha\beta$-frame single-tone sinusoidal perturbation magnitude is 1% of the system nominal voltage, DFT window size is 1 second, and the convergence tolerance is 0.5%. The $\alpha\beta$-scan is performed for 1–59 Hz frequency range with 1 Hz resolution.

For accuracy validation of $\alpha\beta$ MIMO IBSA, dq-scan is also performed with the same procedure of $\alpha\beta$-scan (see Section 2.1). The voltage perturbation magnitude, DFT window size and convergence tolerance are also same in both $\alpha\beta$- and dq-scans. To perform dq MIMO IBSA, the sequence domain grid side impedances are also transformed into dq-frame using:

$$\mathbf{Z}_{dq}^{\mathbf{Grid}}(f_i) = \mathbf{C}^{-1} \cdot diag\left(\left[Z_p^{Grid}(j\omega_i + j\omega_b) \quad Z_n^{Grid}(j\omega_i - j\omega_b)\right]\right) \cdot \mathbf{C} \tag{7}$$

3.1. DFIG-based WP series capacitor SSI

The $\alpha\beta$ admittance of the DFIG-based WP ($\mathbf{Y}_{\alpha\beta}^{\mathbf{WP}}(f_i)$) and the $\alpha\beta$ impedance of grid ($\mathbf{Z}_{\alpha\beta}^{\mathbf{Grid}}(f_i)$) are presented in Fig. 3(a) and (b). As seen in Fig. 3(a) $\mathbf{Y}_{\alpha\beta}^{\mathbf{WP}}(f_i)$ meets:

$$Y_{\alpha\alpha}^{WP}(f_i) = Y_{\beta\beta}^{WP}(f_i), \quad Y_{\alpha\beta}^{WP}(f_i) = -Y_{\beta\alpha}^{WP}(f_i), \tag{8}$$

As the off-diagonal elements of grid meet $Z_{\alpha\beta}^{Grid}(f_i) = Z_{\beta\alpha}^{Grid}(f_i) = 0$, they are not presented in Fig. 3(b). $\mathbf{Z}_{\alpha\beta}^{\mathbf{Grid}}(f_i)$ meets

$$Z_{\alpha\alpha}^{Grid}(f_i) = Z_{\beta\beta}^{Grid}(f_i) \tag{9}$$

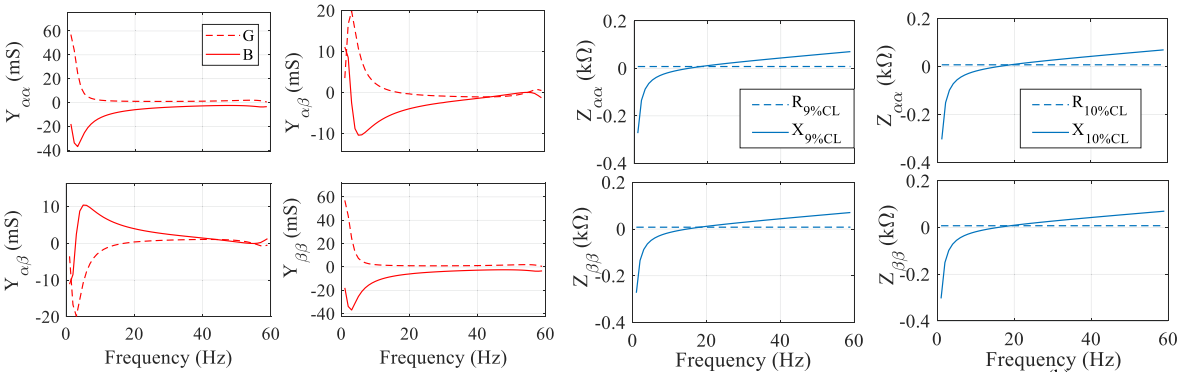

(a) αβ admittance of the DFIG-based WP

(b) αβ impedances of the grid side subsystem in cases 1 and 2

Fig. 3. The obtained (a) WP $\alpha\beta$ admittance (G, B, real and imaginary components of WP admittances, respectively) and (b) grid $\alpha\beta$ impedances.

The eigenloci of $\mathbf{Z}_{\alpha\beta}^{\mathbf{Grid}}(f) \cdot \mathbf{Y}_{\alpha\beta}^{\mathbf{WP}}(f)$ and the Bode plot of $F_{C1}(s)$ for cases 1 and 2 are shown in Fig. 4(a)–(d). The corresponding stability margin and resonance frequency (f_r) are shown in Table 2.

Table 2. IBSA results of the DFIG based WP series capacitor SSI.

Case	$\alpha\beta$-scan		dq-scan	
	f_r (Hz)	Stability margin	f_r (Hz)	Stability margin
1	$f_{\text{Mag}} = 6.4$ $f_{\text{Ang}} = \backslash$	PM $= 4.0°$ GM $=$ Infinity	$f_{\text{Mag}} = 6.3$ $f_{\text{Ang}} = \backslash$	PM $= 4.8°$ GM $=$ Infinity
2	$f_{\text{Mag}} = 6.6$ $f_{\text{Ang}} = 6.4$	PM $= -1.7°$ GM $= -1.9$ dB	$f_{\text{Mag}} = 6.6$ $f_{\text{Ang}} = 6.5$	PM $= -1.5°$ GM $= -1.6$ dB

Note: f_{Mag} and f_{Ang} are the identified resonance frequencies with $|\mathbf{Z}_{\alpha\beta}^{\text{Grid}}(f) \cdot \mathbf{Y}_{\alpha\beta}^{\text{WP}}(f)| = 1$ and $ang(\mathbf{Z}_{\alpha\beta}^{\text{Grid}}(f) \cdot \mathbf{Y}_{\alpha\beta}^{\text{WP}}(f)) = -180°$, respectively.

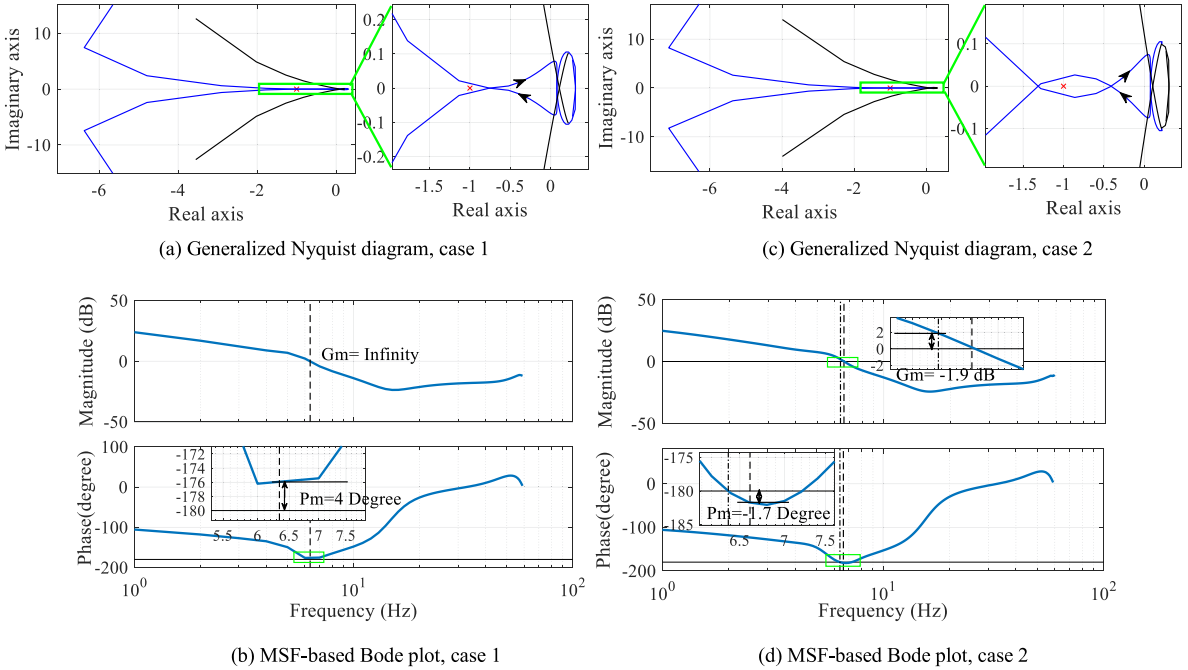

(a) Generalized Nyquist diagram, case 1

(c) Generalized Nyquist diagram, case 2

(b) MSF-based Bode plot, case 1

(d) MSF-based Bode plot, case 2

Fig. 4. IBSA for cases 1 and 2.

According to the generalized Nyquist diagram and Bode plot analysis presented in Fig. 4(a) and (b), case 1 is stable. On the other hand, the encirclement of $(-1, j0)$ in Fig. 4(c) indicates instability in case 2. The phase margin (PM), gain margin (GM) and resonance frequency of the system are calculated using the Bode plots and presented in Table 2 together with the dq MIMO IBSA results. Both Table 2 and the EMT simulation results presented in Fig. 5 confirm the accuracy of the $\alpha\beta$ MIMO IBSA: The oscillation in WP active power is damped in case 1 (Fig. 5(a)), and no oscillation components are found in the voltage frequency spectrum (VFS) (see Fig. 5(b)); In Fig. 5(c), sustained oscillations are observed in active power due to controller saturation, 7 Hz oscillation component is found in the VFS in Fig. 5(d).

3.2. FSC-based WP series capacitor SSI

The generalized Nyquist diagram shown in Fig. 6(a) does not encircle $(-1, j0)$, and the Bode plot shown in Fig. 6(b) indicates a critical stable condition in Case 3 with very small PM and GM. The resonance frequency, PM, and GM obtained with the Bode plot are shown in Table 3. The dq MIMO IBSA produces similar results which are also presented in Table 3. It should be noted that SISO IBSA indicates instability in case 3 in [22]. On the other hand, encirclement of $(-1, j0)$ in Fig. 6(c) and the negative PM and GM determined by the Bode plot in Fig. 6(d)

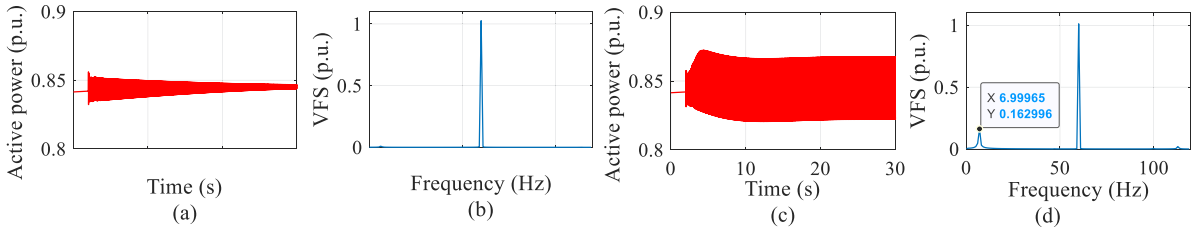

Fig. 5. EMT simulation results: (a) WP output active power in case 1, (b) WP phase a VFS in case 1, (c) WP output active power in case 2, (d) WP phase a VFS in case 2.

Table 3. IBSA results of the FSC-based WP series capacitor SSI.

Case	$\alpha\beta$-scan		dq-scan	
	f_r (Hz)	Stability margin	f_r (Hz)	Stability margin
3	$f_{\text{Mag}} = 2.5$ $f_{\text{Ang}} = 2.7$	PM $= 0.6°$ GM $= 1.9$ dB	$f_{\text{Mag}} = 2.5$ $f_{\text{Ang}} = 2.6$	PM $= 1.0°$ GM $= 1.4$ dB
4	$f_{\text{Mag}} = 4.0$ $f_{\text{Ang}} = 1.7$	PM $= -8.1°$ GM $= -13.2$ dB	$f_{\text{Mag}} = 3.7$ $f_{\text{Ang}} = 1.5$	PM $= -7.8°$ GM $= -12.7$ dB

indicate case 4 is unstable. The EMT simulation results confirm the accuracy of the $\alpha\beta$ MIMO IBSA: the damped and sustained oscillations in WP active power are presented in Fig. 7(a) and (c), indicate cases 3 and 4 are stable and unstable, respectively. 3 Hz dominant and 117 Hz mirror frequency components are found in the WP VFS in Fig. 7(d).

The total EMT simulation time of $\alpha\beta$- and dq-scans for 1–59 Hz range with 1 Hz resolution are presented in Table 4. All simulations were performed on a desktop PC with the following specifications: CPU (Intel Core i5-7600 3.50 GHz), 16 GB RAM, 64-bit operating system. The $\alpha\beta$-scan usage reduces the total simulation time (compared to dq-scan) 9% and 36% in DFIG and FSC-based WP, respectively.

Table 4. Simulation time of $\alpha\beta$- and dq-scan (1–59 Hz).

WP type	Simulation time (s)	
	$\alpha\beta$-scan	dq-scan
DFIG	3615	3957
FSC	1207	1878

4. Conclusion

This paper proposed a $\alpha\beta$-scan method to obtain the $\alpha\beta$ MIMO impedance and its usage in IBSA. The accuracy of $\alpha\beta$ MIMO IBSA was validated by comparing with dq MIMO IBSA and EMT simulations on series capacitor SSI cases with different type IBRs (DFIG- and FSC-based WPs). The $\alpha\beta$ MIMO IBSA offers similar accuracy with dq MIMO IBSA. As the $\alpha\beta$-scan is conducted in stationary frame, it has the following advantages over the dq-scan:

(1) The $\alpha\beta$-scan usage reduces the total simulation time (compared to dq-scan) by 9% and 36% in DFIG- and FSC- based WPs, respectively.

(2) The $\alpha\beta$ MIMO IBSA inherently differentiates the resonance and mirror frequencies, which is the major drawback in dq-scan method.

Hence, it is a better alternative to dq-scan and the associated dq MIMO IBSA.

This paper also used an MSF-based method for the first time in IBSA of SSI to achieve Bode plot-based analysis for providing better visualized presentation of resonance frequency and stability margins compared to the GNC.

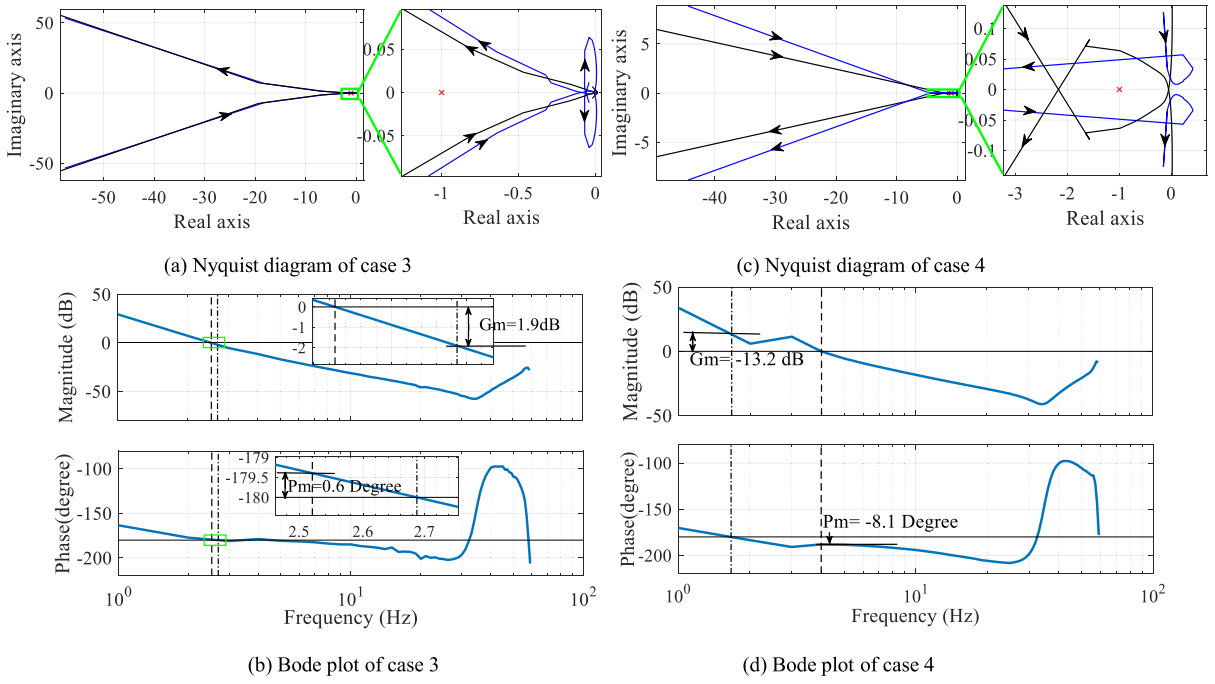

Fig. 6. IBSA of scenarios 3 and 4.

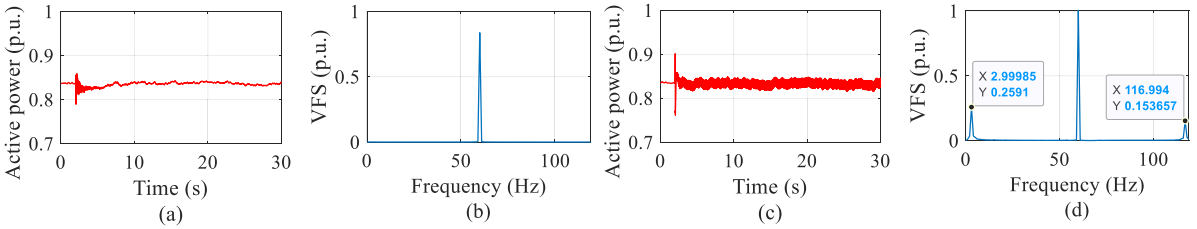

Fig. 7. EMT simulations of cases 3 and 4. (a), (b) WP output active power and WP VFS (phase a) of case 3. (c), (d) WP output active power and WP VFS (phase a) of case 4.

Declaration of competing interest

The authors declare no conflict of interest.

Data availability

Data will be made available on request.

Acknowledgments

This work was supported by the Hong Kong Research Grant Council for the Research Project under Grant 25223118.

References

[1] Y. Cheng, et al., Real-world subsynchronous oscillation events in power grids with high penetrations of inverter-based resources, IEEE Trans Power Syst (2022).

[2] Jan. Shair, Xiaorong. Xie, Wei. Liu, Xuan. Li, Haozhi. Li, Modeling and stability analysis methods for investigating subsynchronous control interaction in large-scale wind power systems, Renew Sustain Energy Rev 135 (2021) 110420.

[3] Y. Cheng, S.H. (Fred) Huang, J. Rose, V.A. Pappu, J. Conto, Subsynchronous resonance assessment for a large system with multiple series compensated transmission circuits, IET Renew Power Gener 13 (1) (2019) 27–32.
[4] U. Karaagac, J. Mahseredjian, S. Jensen, R. Gagnon, M. Fecteau, I. Kocar, Safe operation of DFIG based wind parks in series compensated systems, IEEE Trans Power Deliv 33 (2) (2018) 709–718.
[5] L. Fan, Z. Miao, An explanation of oscillations due to wind power plants weak grid interconnection, IEEE Trans Sustain Energy 9 (1) (2018) 488–490.
[6] L. Fan, C. Zhu, Z. Miao, M. Hu, Modal analysis of a DFIG-based wind farm interfaced with a series compensated network, IEEE Trans Energy Convers 26 (4) (2011) 1010–1020.
[7] N. Pogaku, M. Prodanovic, T.C. Green, Modeling, Analysis and testing of autonomous operation of an inverter-based microgrid, IEEE Trans Power Electron 22 (2) (2007) 613–625.
[8] R. Middlebrook, Input filter considerations in design and application of switching regulators, in: IEEE ind. appl. soc. annu. meet., 1997, pp. 1–6.
[9] M. Belkhayat, Stability criteria for ac power systems with regulated loads (Ph.D. dissertation), Purdue Univ. West Lafayette, IN, USA, 1997.
[10] M. Cespedes, J. Sun, Impedance modeling and analysis of grid-connected voltage-source converters, IEEE Trans Power Electron 29 (3) (2014) 1254–1261.
[11] B. Badrzadeh, M. Sahni, D. Muthumuni, Y. Zhou, A. Gole, Sub-synchronous interaction in wind power plants –part I: Study tools and techniques, in: IEEE power and energy society general meeting, San Diego, California, USA, 2012, pp. 1–9.
[12] B. Badrzadeh, M. Sahni, Y. Zhou, D. Muthumuni, A. Gole, General methodology for analysis of sub-synchronous interaction in wind power plants, IEEE Trans Power Syst 28 (2) (2013) 1858–1869.
[13] Y. Cheng, M. Sahni, D. Muthumuni, B. Badrzadeh, Reactance scan crossover-based approach for investigating SSCI concerns for DFIG-based wind turbines, IEEE Trans Power Deliv 28 (2) (2013) 742–751.
[14] N. Watson, J. Arrillaga, Power systems electromagnetic transients simulation, 1st ed., IET, London, UK, 2003.
[15] Xiaorong Xie, Yipeng. Dong, Kai. Bai, Xun. Gao, Ping. Liu, The improved SSR electromagnetic simulation model and its comparison with field measurements, in: SIMULTECH 2012, Rome, Italy, 2012, pp. 419–424.
[16] W. Ren, E. Larsen, A refined frequency scan approach to sub-synchronous control interaction (SSCI) study of wind farms, IEEE Trans Power Syst 31 (5) (2016) 3904–3912.
[17] G. Francis, R. Burgos, D. Boroyevich, F. Wang, K. Karimi, An algorithm and implementation system for measuring impedance in the D-Q domain, in: 2011 IEEE energy conversion congress and exposition, 2011, pp. 3221–3228.
[18] Y.L. Familiant, K.A. Corzine, J. Huang, M. Belkhayat, AC impedance measurement techniques, in: IEEE international conference on electric machines and drives, 2005, pp. 1850–1857.
[19] J. Huang, K.A. Corzine, Ac impedance measurement by line-to-line injected current, in: 2006 IEEE industry applications conference forty-first IAS annual meeting, 2006, pp. 300–306.
[20] J. Huang, K.A. Corzine, M. Belkhayat, Small-signal impedance measurement of power-electronics-based AC power systems using line-to-line current injection, IEEE Trans Power Syst 24 (2) (2009) 445–455.
[21] B. Wen, D. Boroyevich, R. Burgos, P. Mattavelli, Z. Shen, Small-signal stability analysis of three-phase AC systems in the presence of constant power loads based on measured d-q frame impedances, IEEE Trans Power Electron 30 (10) (2015) 5952–5963.
[22] A.S. Trevisan, Â. Mendonça, R. Gagnon, J. Mahseredjian, M. Fecteau, Analytically validated SSCI assessment technique for wind parks in series compensated grids, IEEE Trans Power Syst 36 (1) (2021) 39–48.
[23] X. Wang, L. Harnefors, F. Blaabjerg, Unified impedance model of grid-connected voltage-source converters, IEEE Trans Power Electron 33 (2) (2018) 1775–1787.
[24] Y. Liao, X. Wang, Stationary-frame complex-valued frequency-domain modeling of three-phase power converters, IEEE J Emerg Sel Top Power Electron 8 (2) (2020) 1922–1933.
[25] A.G.J. MacFarlane, I. Postlethwaite, The generalized nyquist stability criterion and multivariable root loci, Internat J Control 25 (1977) 81–127.
[26] W.E. Leithead, J. O'Reilly, Multivariable control by individual channel design: an automotive gas turbine case study, in: International conference on control 1991, Edinburgh, UK, pp. 1261–1266.
[27] L.A. Amézquita-Brooks, C.E. Ugalde-Loo, E. Licéaga-Castro, J. Licéaga-Castro, The multivariable structure function as an extension of the RGA matrix: relationship and advantages, Cybern Phys 2 (2) (2013) 53–62.
[28] G.C. Paap, Symmetrical components in the time domain and their application to power network calculations, IEEE Trans Power Syst 15 (2) (2000) 522–528.
[29] J. Sun, Impedance-based stability criterion for grid-connected inverters, IEEE Trans Power Electron 26 (11) (2011) 3075–3078.
[30] U. Karaagac, J. Mahseredjian, R. Gagnon, H. Gras, et al., A generic EMT-type model for wind parks with permanent magnet synchronous generator full size converter wind turbines, IEEE Power Energy Technol Syst J 6 (3) (2019) 131–141.
[31] U. Karaagac, J. Mahseredjian, H. Gras, H. Saad, J. Peralta, L.D. Bellomo, Simulation models for wind parks with variable speed wind turbines in EMTP-RV, Research report, Polytechnique Montréal, 2016.
[32] A. Haddadi, I. Kocar, T. Kauffmann, U. Karaagac, E. Farantatos, J. Mahseredjian, Field validation of generic wind park models using fault records, J Mod Power Syst Clean Energy 7 (4) (2019) 826–836.
[33] IEEE-PES Wind SSO Task Force, Wind energy systems sub-synchronous oscillations: events and modeling, Technical report, PES-TR80, AMPS Committee, 2020.
[34] J. Mahseredjian, S. Dennetière, et al., On a new approach for the simulation of transients in power systems, Electr Power Syst Res 77 (11) (2007) 1514–1520.